ACS Sustainable Chemistry & Engineering

Research Article

Cite This: ACS Sustainable Chem. Eng. 2020, 8, 179−189

pubs.acs.org/journal/ascecg

Electroreduction of Carbon Dioxide into Selective Hydrocarbons at Low Overpotential Using Isomorphic Atomic Substitution in Copper Oxide

Subramanian Nellaiappan,[†] Ritesh Kumar,[‡] C. Shivakumara,[§] Silvia Irusta,[∥] Jordan A. Hachtel,[⊥] Juan-Carlos Idrobo,[⊥] Abhishek K. Singh,[‡] Chandra Sekhar Tiwary,[#] and Sudhanshu Sharma*[,†]

[†]Department of Chemistry, Indian Institute of Technology Gandhinagar, Palaj, Gandhinagar 382355, Gujarat, India
[‡]Materials Research Center and [§]Solid State and Structural Chemistry Unit, Indian Institute of Science, Bangalore 560012, India
[∥]Department of Chemical Engineering, Nanoscience Institute of Aragon (INA), University of Zaragoza, Zaragoza 50018, Spain
[⊥]Center for Nanophase Materials Sciences, Oak Ridge National Laboratory, Oak Ridge, Tennessee 37830, United States
[#]Metallurgical and Materials Engineering, Indian Institute of Technology, Kharagpur 600036, India

Supporting Information

ABSTRACT: The conversion of carbon dioxide into selective hydrocarbons is vital for green energy generation. Due to the chemical instability and lower activity, environmentally stable transition metal oxides (e.g., CuO) are unpopular for CO_2 electroreduction catalysis. Here, we demonstrate substitution of Cu with an isomorphic atom, i.e., Ni, in CuO and utilize it for improving the hydrocarbon selectivity by 4 times as compared to that of pristine CuO. Hydrocarbon formation is achieved at the lowest possible applied potential (−0.2 V, reversible hydrogen electrode). This gives the overpotential of about 0.37 V for methane and 0.28 V for ethylene, the lowest ever reported. Employing the ionic interaction between Ni and Cu, this catalyst suppresses the hydrogen evolution reaction to improve the hydrocarbon selectivity prominently. It is observed that current normalized by the Brunauer−Emmett−Teller surface area gives 15−20 times enhancement in the case of Ni-substituted CuO compared to undoped CuO. The in situ experiments indicate that Ni-doped CuO prefers CO pathways compared to formate, resulting into high hydrocarbon selectivity. The experimental observation is further supported by density functional theory studies, which reveal that the Ni-doped CuO catalyst has a higher limiting potential for CO_2 electroreduction to CH_4 due to the stabilization of the CH_2O intermediate on the $Cu_{0.9375}Ni_{0.0625}O$ surface rather than the CHO intermediate, in comparison to the pristine CuO surface.

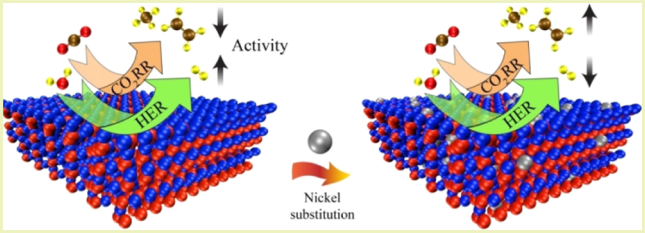

KEYWORDS: *redox-active catalyst, isomorphic atomic substitution, nickel-substituted copper oxide, CO_2 electroreduction, FTIR and DFT studies*

INTRODUCTION

Conversion of CO_2 into value-added products is beneficial for both environment and energy.[1,2] Alongside thermocatalytic[3] and photochemical,[4,5] electrochemical conversion of CO_2 has attracted much interest due to its efficient production of a variety of gaseous and liquid products under ambient temperature and pressure.[2,6,7] Among these numerous products, C_1- and C_2-hydrocarbons (CH_4 and C_2H_4) are exceptionally attractive but remain elusive due to their high energy densities. In particular, ethylene is highly valuable as it is a key material for manufacturing of polyethylene.[8] There are many challenges associated with the electrochemical reduction of CO_2 such as large overpotential and unavoidable competition with hydrogen evolution reactions (HERs) in an aqueous environment.[9]

Considerable effort has been devoted to develop new catalysts, which can promote CO_2 electroreduction activity with high efficiency and selectivity while suppressing the competing HER. Several heterogeneous catalysts have been developed to improve the electrocatalytic activity by modifying the bulk surface to nanostructures focusing on Cu,[10−13] Ni,[14] Au,[15] Ag,[16] Sn,[17] In,[18] and Pd.[19] Of these, Cu is unique as being the only material to convert CO_2 into hydrocarbons with high faradaic efficiency,[10−13] but it has high overpotential, shows wide product distribution, and leads to undesired hydrogen evolution reaction. To overcome these challenges, Cu has been alloyed with other metals,[20−24] used as oxides,[25−28] used as derived from metal oxides,[29−31] and used as the supported catalyst[32−34] for enhanced electrochemical reduction of CO_2 into desired products. The reasons behind the catalytic activities of these oxides are optimum

Received: August 28, 2019
Revised: November 13, 2019
Published: November 22, 2019

Downloaded via INDIAN INST OF SCIENCE on January 14, 2023 at 10:24:16 (UTC).
See https://pubs.acs.org/sharingguidelines for options on how to legitimately share published articles.

© 2019 American Chemical Society

DOI: 10.1021/acssuschemeng.9b05087
ACS Sustainable Chem. Eng. 2020, 8, 179−189

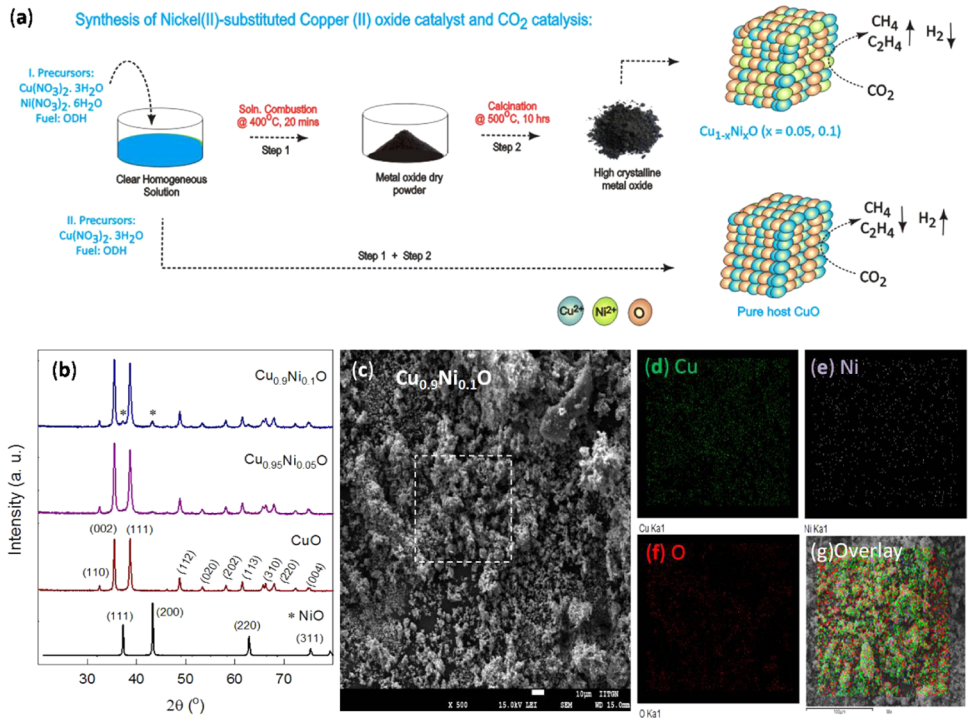

Figure 1. Schematic representation for the synthesis of Ni-substituted CuO and pure host CuO catalysts using the solution combustion method (a); comparative X-ray diffraction (XRD) patterns of $Cu_{0.9}Ni_{0.1}O$, $Cu_{0.95}Ni_{0.05}O$, CuO, and NiO catalysts (b); field emission scanning electron microscopy (FESEM) image of $Cu_{0.9}Ni_{0.1}O$ (c); and energy-dispersive X-ray spectroscopy (EDS) elemental mapping for Cu Kα (d), Ni Kα (e), O Kα (f), and its overlay (g) images.

binding energy of reaction intermediates,[25−28] multiple valence metals,[29−31] and synergetic effect.[32−34]

It is well-known that replacing a small fraction of the isomorphic cations in a host metal oxide with a different cation (doping) can change the electrochemical performance of the metal oxide catalyst due to its synergetic effect.[35,36] Adopting the similar substitutional chemistry, we developed a new electrocatalyst by substitution of isomorphic nickel (Ni^{2+} cation; as dopant) on copper(II) oxide (CuO as host) using the solution combustion method. Nickel and copper in their metallic state have highly similar overpotentials for CO_2 electroreduction; therefore, it is expected that synergy between the two in the ionic state can tune the electrocatalytic activity. By exploiting the efficient ionic interaction between Cu and Ni, we effectively enhance both CO_2 electroreduction and the hydrocarbon selectivity. This is a new strategy and has not been explored previously.

EXPERIMENTAL SECTION

Synthesis. The solution combustion method has been widely known for preparing the doped metal oxides and simple metal oxides because of its rapidness and large yield of the final product with high crystallinity. In a typical preparation of Ni-doped CuO ($Cu_{1-x}Ni_xO$; x = 0.05 and 0.1), 2.57 g (x = 0.05) or 2.72 g (x = 0.1) of oxalyldihydrazide (ODH) was dissolved in hot deionized water. This is followed by the addition of 5.0 g of $Cu(NO_3)_2{\cdot}3H_2O$ (99.9% purity) and 0.32 g (x = 0.05) or 0.67 g (x = 0.1) of $Ni(NO_3)_2{\cdot}6H_2O$ (99.9% purity) to make a clear solution. For CuO, 2.44 g of ODH and 5.0 g of $Cu(NO_3)_2{\cdot}3H_2O$ were used. For NiO, 2.03 g of ODH and 5.0 g of $Ni(NO_3)_2{\cdot}6H_2O$ were used. Further, the solution was stirred using a glass rod and evaporated by heating at 70 °C until we get a homogeneous solution. The as-prepared clear solution was placed in a muffle furnace preheated at 400 °C for 20 min. Then, the dish was cooled and powder was collected in a crucible, which was kept for calcination at 500 °C for 10 h (Figure 1a). For NiO-deposited CuO (NiO/CuO), 200 mg of as-prepared CuO and 73.5 mg of $NiNO_3.6H_2O$ (equivalent to 10% Ni in $Cu_{0.9}Ni_{0.1}O$) are dispersed in 10 mL of Millipore water followed by sonication for 30 min. Further, 2 mL of 1.0 M KOH was added dropwise until precipitation starts, followed by leaving it for 1 h. The precipitate was washed thoroughly with water, filtered, and dried at 80 °C. A final calcination step was carried out at 350 °C for 10 h to convert nickel hydroxide into nickel oxide. Likewise, Ni-deposited CuO (Ni/CuO) was synthesized by the chemical reduction method. Briefly, 200 mg of as-prepared CuO with 73.5 mg of $NiNO_3.6H_2O$ (equivalent to 10% Ni in $Cu_{0.9}Ni_{0.1}O$) was dispersed in 10 mL of Millipore water. Then, 1 mL of 99% hydrazine hydrate solution was added dropwise to reduce nickel nitrate into nickel metal. The obtained compound was washed, filtered, and kept for drying at 80 °C for 4 h.

Instrumentation. Combustion-synthesized Ni-doped CuO ($Cu_{0.9}Ni_{0.1}O$ and $Cu_{0.95}Ni_{0.05}O$) and CuO have been characterized by powder X-ray diffraction (XRD), Rietveld refinement, Brunauer−Emmett−Teller (BET) surface area measurement, field emission scanning electron microscopy (FESEM-EDS), high-resolution transmission electron microscopy (HRTEM-EDS), and X-ray photoelectron spectroscopy (XPS). Powder XRD was carried out using a Bruker D8 Discover diffractometer (Germany) in the range of 20−80° to the crystal phases. The Rietveld refinement was done using the FullProf-fp2k program varying 17 parameters simultaneously such as the overall scale factor and background parameter. BET measurement was carried out in Micrometrics 3Flex. Samples were degassed under vacuum at 150 °C before the analysis. High-resolution scanning electron microscopy was performed using JEOL (JSM7600F) with energy-dispersive spectroscopy (Oxford, Model INCA Energy 250 EDS). The high-resolution transmission electron micrographs were acquired using an FEI Titan Themis (s) transmission electron microscope. XPS was performed with Axis Ultra DLD (Kratos Analytical Limited). The spectra were obtained using the monochromatized Al Kα source (1486.6 eV) run at 15 kV and 10 mA. For the individual peak regions, pass energy of 20 eV was used. Survey spectrum was measured at 160 eV pass energy. Analysis of the peaks

DOI: 10.1021/acssuschemeng.9b05087
ACS Sustainable Chem. Eng. 2020, 8, 179−189

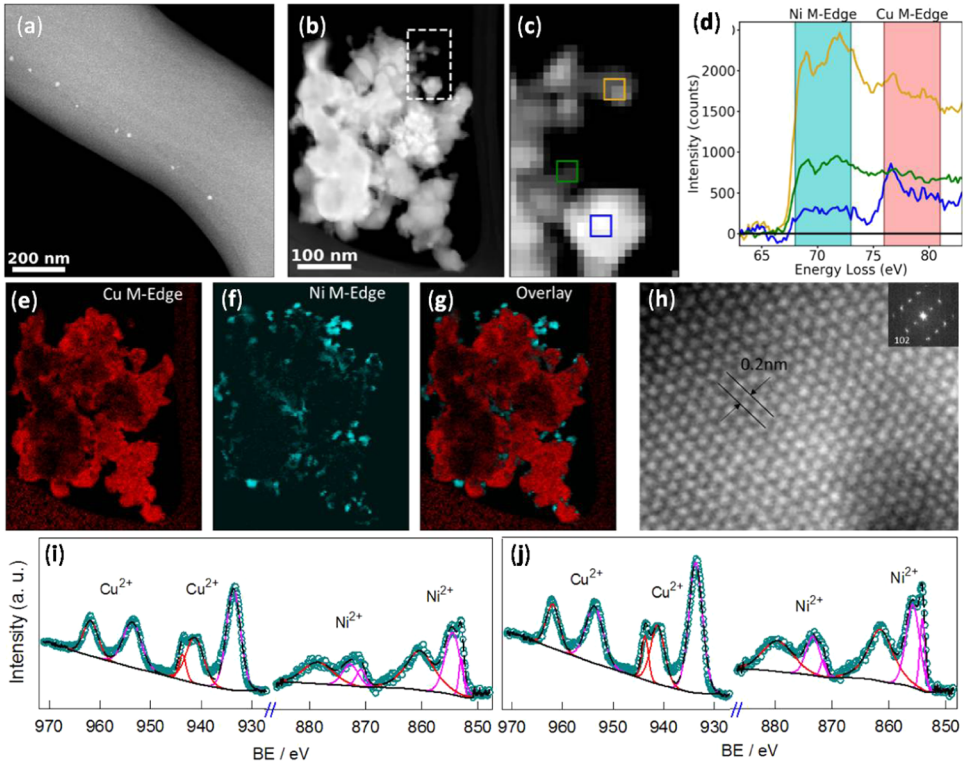

Figure 2. HRTEM image of $Cu_{0.9}Ni_{0.1}O$ (a) along with the STEM images (b, c), EELS signals (d), EDS elemental mapping for Cu M-edge (e), Ni M-edge (f), overlay (g), and high-resolution planar image with its Fourier transform in the inset (h). Comparative high-resolution XPS Cu(2p) and Ni(2p) spectra of $Cu_{0.95}Ni_{0.05}O$ (i) and $Cu_{0.9}Ni_{0.1}O$ (j) catalysts.

was performed with Casa XPS software, using a weighted sum of Lorentzian and Gaussian component curves after Shirley background subtraction. The binding energies were referenced to the internal C (1s) (284.9 eV) standard.

Electrochemical Studies and Product Analysis. Electrochemical studies were performed using the conventional three-electrode system at CHI660E electrochemical workstation. All solutions were prepared using double-distilled water. The working electrode was made by mixing 100 mg of the prepared catalyst and 200 μL of 5% Nafion solution as a binder. After that, 300 μL of isopropanol was added to it to make thin slurry followed by deposition on a glassy carbon working electrode (GCE). The geometric area of the electrode was 0.071 cm^2. A platinum wire was used as the counter electrode, the Ag/AgCl (saturated KCl) electrode was used as the reference electrode, and 0.5 M $NaHCO_3$ was used as the supporting electrolyte. The estimated uncompensated resistance in the cell was 134.1 ohm. The conversion of potential to reversible hydrogen electrode (RHE) was calculated using the following equation: E (RHE) = E (Ag/AgCl) + (0.196 + 0.059 pH). Measurements of electroreduction of CO_2 were carried out using the CO_2-saturated 0.5 M $NaHCO_3$ (pH = 6.8) electrolyte, i.e., after CO_2 purging for 30 min under room temperature.

An air-tight electrochemical cell was used for the gaseous product formation and analysis. For quantification of gaseous products, a gas-tight syringe (Hamilton, 1000μL) was used to transfer the evolved gases into a gas chromatograph (GC; CIC Baroda). A Haysep-A column was used for separation, and a flame ionization detector was used for detection of CO and hydrocarbons. A thermal conductivity detector was used for H_2 detection. A standard gas mixture was used for calibrating the GC. For liquid products, gas chromatograph (Agilent 7890) was used.

The faradaic efficiency (FE %) was calculated based on eq 1

$$\mathrm{FE}\% = \frac{n \times F \times N}{Q} \times 100 \qquad (1)$$

where n is the number of electrons transferred in the faradaic process; F is the Faraday constant, 96485 C mol^{-1}; N is the amount of the generated product in this process; and Q is the total charge passed through the whole reaction.

In Situ Fourier Transform Infrared (FTIR) Spectroscopy under Gaseous Environment. Diffuse reflectance infrared Fourier transform spectroscopy (DRIFTS) experiments were performed with CuO and $Cu_{0.9}Ni_{0.1}O$ (mixture of KBr) under different gaseous compositions and at different temperatures using a Thermo Scientific NICOLET-iS50 FTIR spectroscope. The DRIFTS cell (Pike Technologies) with an environmental chamber was used to record the IR spectra. The cell was first purged with ultra-high-purity nitrogen (UHP N_2). All of the experiments were carried out at a fixed flow rate of 20 mL min^{-1}, which is controlled by a mass flow controller. The catalysts were first heated from room temperature to 200 °C and then cooled to room temperature in UHP N_2. FTIR spectra were then recorded at different temperatures in the presence of different gases. A spectrum of powdered KBr was recorded in UHP N_2 at room temperature and 100 °C, which served as the background at room temperature and higher temperatures.

Computational Methodology. Density functional theory (DFT) was used for theoretical calculations, implemented in the Vienna ab initio simulation package.[37] Dudarev's approach was utilized for treating the localized nature of electrons in the d orbitals of transition metal oxides.[38] The electron−ion interactions were described using all-electron projector augmented wave pseudopotentials, and Perdew−Burke−Ernzerhof generalized gradient approximation[39] was used to approximate electronic exchange and correlations. The Brillouin zone was sampled using 10 × 12 × 8 and 5 × 4 × 1 Monkhorst−Pack k-grids for the bulk and slab calculations, respectively. All structures were relaxed using a conjugate gradient scheme until the energies and each component of the forces converged to 10^{-5} eV and 0.01 eV $Å^{-1}$, respectively. The (111) surface of CuO was generated from its optimized bulk structures using Virtual Nano Lab version 2016.2. The structure of $Cu_{0.9375}Ni_{0.0625}O$ random alloy was generated from the CuO(111) surface using the

DOI: 10.1021/acssuschemeng.9b05087
ACS Sustainable Chem. Eng. 2020, 8, 179−189

Alloy Theoretic Automated Toolkit (ATAT) code.[40] The structure had four layers of atoms with the bottom three layers frozen and allowing only the topmost layer to relax, to mimic the bulk behavior. For both Cu and Ni atoms, the values of U (Hubbard parameter) and J (on-site Coulomb interaction) were taken to be 7.5 and 1, respectively. The vibrational frequencies were calculated by employing density functional perturbation theory.

RESULTS AND DISCUSSION

Characterizations. Figure 1b shows the comparative powder X-ray diffraction patterns of $Cu_{0.9}Ni_{0.1}O$, $Cu_{0.95}Ni_{0.05}O$, CuO, and NiO. Intense and sharp peaks suggest that the obtained electrocatalysts are crystalline. In the case of $Cu_{0.95}Ni_{0.05}O$, no additional significant peak corresponding to the Ni metal or NiO is observed, confirming the substitution of Ni in host CuO and forming solid solution. XRD of $Cu_{0.9}Ni_{0.1}O$ shows two additional new peaks related to NiO, indicating that a phase like $NiO/Cu_{1-x}Ni_xO$ is formed. The presence of some metallic Ni can also not be ruled out, which may be present in low concentration with size in nano range, not detectable in the XRD. XRD of Ni/CuO and NiO/CuO can be seen in Figure S1a in the Supporting Information. Both Ni/CuO and NiO/CuO show peaks related to the Ni metal and nickel oxide, and these are considered as the supported catalysts. Rietveld refinement is carried out to estimate the correctness of the phase and change in the lattice parameter/volume after the doping. Figure S1b–d displays the observed, calculated, and difference plot for $Cu_{0.9}Ni_{0.1}O$, $Cu_{0.95}Ni_{0.05}O$, and CuO, respectively. The Rietveld refined plot of $Cu_{0.95}Ni_{0.05}O$ shows closeness between calculated and observed patterns. All of the parameters estimated after Reitveld refinements are shown in Supporting Information Table S1. Considerable decrease in the lattice parameter of CuO after the Ni doping is observed. This agrees with the smaller size of the Ni^{2+} ion than the Cu^{2+} ion. As a result of decrease in the lattice parameter, there is a decrease in the total lattice volume, confirming the bulk doping of Ni^{2+} in the CuO host. Lattice shrinking will also have contribution from lattice strain and defects, which will prevent validation of Vegard's law. Surface areas of all of the samples are measured by the BET method, and the surface area values are 0.58, 0.74, and 1.7 $m^2\ g^{-1}$ for $Cu_{0.95}Ni_{0.05}O$, $Cu_{0.9}Ni_{0.1}O$, and CuO, respectively. The surface area for both NiO/CuO and Ni/CuO is 5.0 $m^2\ g^{-1}$.

The surface morphology and composition of $Cu_{0.9}Ni_{0.1}O$ are studied using FESEM and HRTEM with EDS mapping. The FESEM along with EDS elemental mapping images of $Cu_{0.9}Ni_{0.1}O$ (Figure 1c–g) confirms the presence of Ni over the CuO host. In addition, the dark field TEM image (Figure 2a) and high-resolution scanning transmission electron microscopy (STEM) image (Figure 2b,c) indicate the cluster nature of $Cu_{0.9}Ni_{0.1}O$. Electron-energy-loss spectra (EELS) are acquired from three individual nanoparticles (indicated in Figure 2c) that show prominent signals from both the Ni and Cu M-edges at 68 and 74 eV, respectively (Figure 2d). The composition of the large cluster shown in Figure 2b is established through EEL-spectrum imaging, where spectra are acquired at each position in the region of interest. The spatial distributions of Ni and Cu are shown in Figure 2e,f, respectively, with the overlay of the two signals plotted in Figure 2g. The spectral imaging confirms the purity of the catalyst, being composed mostly of Cu with small fractions of Ni. The high-resolution planar TEM image of $Cu_{0.9}Ni_{0.1}O$ shows uniform arrangements of atoms and well-defined lattice fringes with its Fourier transform in the inset (Figure 2h) confirming the crystallinity with an interplanar distance of 0.2 nm and (102) planes. We do observe other binding states of Cu and Ni, which can be attributed to surface Ni/Cu atoms, vacancy, and defects present in samples. Such Ni and Cu atoms may also contribute in chemical reactions as a minor contributor. The above composition studies confirm the presence of Ni, Cu, and Ni-substituted Cu homogeneous regions of $Cu_{0.9}Ni_{0.1}O$.

Further, core XPS spectra of Cu(2p) and Ni(2p) in $Cu_{0.95}Ni_{0.05}O$ and $Cu_{0.9}Ni_{0.1}O$ are shown in Figure 2i,j. In both cases, the doublet of Cu(2p) showed two peaks with binding energies of 933.3 and 953.4 eV, which are due to Cu ($2p_{3/2}$) and Cu ($2p_{1/2}$) of CuO, respectively.[41,42] Relatively higher binding energy peaks at 941.3 and 943.6 eV are shakeup satellite peaks for Cu ($2p_{3/2}$), and the peak at 961.8 eV is the shakeup satellite peak for Cu ($2p_{1/2}$). Likewise, the binding energy of Ni(2p), after deconvolution, is found as the doublet of Ni ($2p_{3/2}$) at 852.9 and 854.5 eV and of Ni ($2p_{1/2}$) at 870.8 and 872.7 eV. Strong shakeup satellite peaks at 860.4 and 878.6 eV also appear as expected.[41,42] The broad peaks at 854.5 and 872.7 eV along with shoulder peaks at 852.9 and 870.8 eV are the unique features of NiO (related to the Ni^{2+} state) and characteristic for bulk nickel oxide.[41,42] All of these peaks collectively confirm the presence of free NiO on the surface. Further, both Cu and Ni are solely in the +2 oxidation state in both the catalysts.

Electrochemical Studies. Initially, continuous cyclic voltammetry (CV) behavior of undoped (CuO and NiO), Ni-substituted CuO ($Cu_{0.95}Ni_{0.05}O$ and $Cu_{0.9}Ni_{0.1}O$), and Ni metal- and NiO-deposited CuO (Ni/CuO and NiO/CuO) drop-casted on a glassy carbon electrode is studied in $NaHCO_3$ (0.5 M). The scan rate is kept at 40 mV s^{-1} for all of the studies. This study is carried out to understand the basic electrochemical properties of the materials. To avoid the oxygen evolution and hydrogen evolution reactions, we restricted our working potential window from −0.8 to 0.4 V vs Ag/AgCl. In Figure 3a, CV of CuO shows a diffused redox peak with enhanced anodic (i_{pa}) and cathodic (i_{pc}) currents compared to the glassy carbon electrode. Oxidation and reduction peaks of Cu^{2+}/Cu^0 appear with the equilibrium potential ($E^{1/2}$) of 144 ± 2 mV with a peak-to-peak separation (ΔE_p) of 197 mV, measured from the last CV cycle. A characteristic pre-wave is also observed at −0.07 V due to the oxidation of Cu^0 to Cu^{1+} (Cu_2O).[32] The surface excess value (Γ), i.e., number of moles of active sites available on the electrode surface, is 0.45 nmol cm^{-2} (Figure S2a), obtained using the following equation: $\Gamma = Q/nFA$.[43] Here, Q is the charge obtained for the redox peak, n is the number of electrons involved, F is the faradaic constant, and A is the area of the electrode. Likewise, $Cu_{0.95}Ni_{0.05}O$ showed similar redox features with $E^{1/2}$ = 137 ± 2 mV and ΔE_p = 184 mV values (Figure 3b), and the calculated Γ value is 0.66 nmol cm^{-2} (Figure S2b). In comparison, CV of $Cu_{0.9}Ni_{0.1}O$ showed prominent redox peaks at 0.051 and −0.192 volts. The enhancement in the anodic and cathodic currents is due to the Cu^{2+}/Cu^0 redox reaction coupled with substituted Ni^{2+}/Ni^0 (Figure 3c). Corresponding $E^{1/2}$ and ΔE_p values are 124 ± 2 and 147 mV with surface excess value (Γ) of 1.17 nmol cm^{-2} (Figure S2c). It is noteworthy that the current values i_{pa} and i_{pc} and surface excess Γ value of $Cu_{0.9}Ni_{0.1}O$ are higher than those of $Cu_{0.95}Ni_{0.05}O$, with slight shifts (~13 ± 2 mV) in the peak

DOI: 10.1021/acssuschemeng.9b05087
ACS Sustainable Chem. Eng. 2020, 8, 179−189

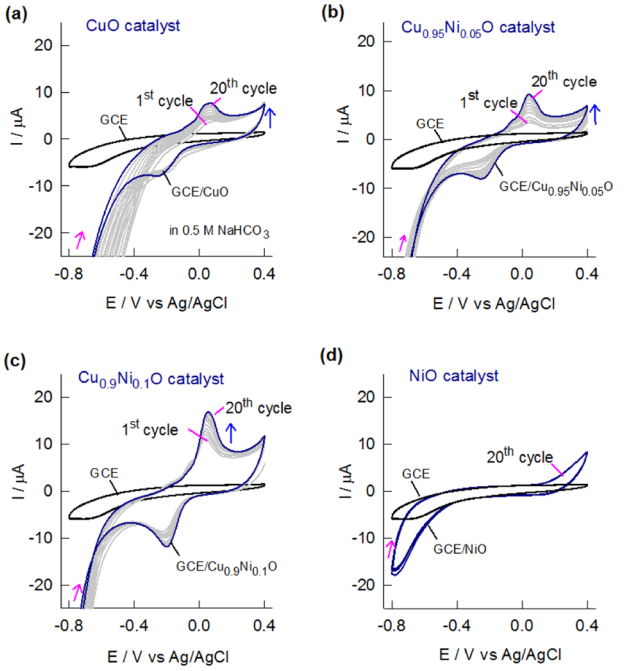

Figure 3. Continuous CV responses of CuO (a) $Cu_{0.95}Ni_{0.05}O$ (b), $Cu_{0.9}Ni_{0.1}O$ (c), and NiO (d) coated GCE along with bare GCE at a scan rate of 40 mV s^{-1} in 0.5 M $NaHCO_3$ electrolyte solution.

potentials. This indicates more number of available active sites in the former due to higher Ni substitution. Comparatively, undoped CuO shows broad and less intense peaks with peak voltages shifted by ~20 mV. Since XRD has shown the presence of a separated NiO phase (Figure 1b), CVs of NiO alone and NiO-deposited CuO (NiO/CuO) are studied in the similar potential range to that in control experiments. No redox feature is observed on NiO (Figure 3d), confirming that the NiO phase is not a redox catalyst in the studied potential range. In the case of NiO/CuO (Figure S2d), CV looks similar to that for CuO (Figure 3c), demonstrating no effect of NiO addition. CV for Ni-metal-supported CuO (Ni/CuO) is also performed as a control experiment (Figure S2e). This is carried out to rule out the presence of any undetected metallic nickel that may be present in the substituted compounds. In the CV, the redox features and the overall response are quite close to CuO with diminished peak intensity. These experiments clearly indicate that the redox electrochemistry is only due to the interaction between substituted Ni^{2+} species and Cu^{2+} and not from the separated Ni/NiO or NiO/CuO phase.

Further, the redox behavior and electron transfer properties of $Cu_{0.9}Ni_{0.1}O$, $Cu_{0.95}Ni_{0.05}O$, and CuO are studied by varying the scan rates from 10 to 150 mV s^{-1} (Figure S3) and potential ranges between $-0.8 \leq 0 \leq 0.8$ V (Figure S4). On increasing scan rates (v), the respective i_{pa} and i_{pc} currents at corresponding redox peaks are increased significantly with a slight shift in E_p and changes in ΔE_p for all three electrocatalysts (Figure S3a–c). Presumably, the potential shifts may be due to the sluggish electron transfer kinetics due to semiconducting nature of the materials. A linear plot of peak current (i_p) versus square root of the scan rate ($v^{1/2}$) is drawn for $Cu_{0.9}Ni_{0.1}O$ (Figure S3d), $Cu_{0.95}Ni_{0.05}O$ (Figure S3e), and CuO (Figure S3f), respectively. The nature of this linearity is directly related to the sufficiently good conductivity of $Cu_{0.9}Ni_{0.1}O$ at the studied scan rates.

In addition, to study the influence of potential window on electrochemical behaviors, the CVs of $Cu_{0.9}Ni_{0.1}O$, $Cu_{0.95}Ni_{0.05}O$, and CuO electrodes are recorded under various potential ranges ($E = -0.8 \leq 0 \leq 0.8$ V) at a scan rate of 40

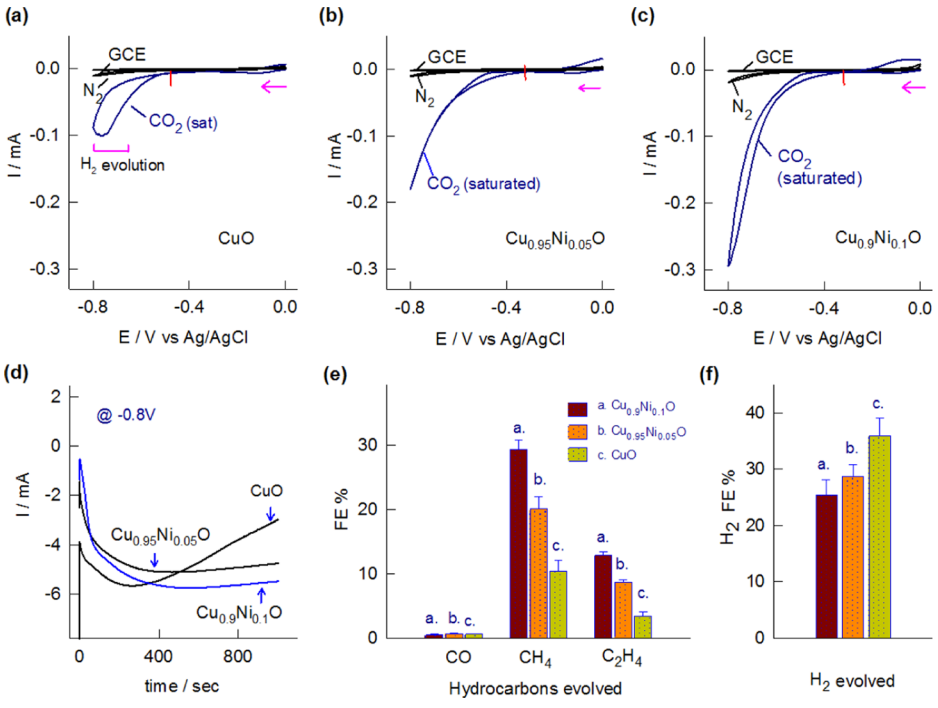

Figure 4. Electroreduction CV response of CuO (a), $Cu_{0.95}Ni_{0.05}O$ (b), and $Cu_{0.9}Ni_{0.1}O$ (c) in CO_2-saturated (for 30 min) 0.5 M $NaHCO_3$ electrolyte solutions at a scan rate of 20 mV s^{-1}. (d) Chronoamperometric responses of CuO, $Cu_{0.95}Ni_{0.05}O$, and $Cu_{0.9}Ni_{0.1}O$ at a fixed potential of −0.8 V vs Ag/AgCl (i.e., −0.2 V RHE) for 1000 s in CO_2-saturated 0.5 M $NaHCO_3$ electrolyte solution. Bar diagrams (with errors) for the faradaic efficiencies of their respective carbonaceous species (e) and hydrogen (f) gaseous products detected in gas chromatography.

DOI: 10.1021/acssuschemeng.9b05087
ACS Sustainable Chem. Eng. 2020, 8, 179−189

mV s^{-1} (Figure S4). In the potential range of −0.4 to +0.4 V, the CVs of $Cu_{0.9}Ni_{0.1}O$ (Figure S4a) and $Cu_{0.95}Ni_{0.05}O$ (Figure S4b) show similar redox features as seen earlier. Once the potential window increased to −0.6 to +0.6 V, the current values i_{pa} and i_{pc} increased for both $Cu_{0.9}Ni_{0.1}O$ and $Cu_{0.95}Ni_{0.05}O$. A wider potential window allows the redox reaction to occur more profoundly, causing the current to increase. This increase in current is more significant in $Cu_{0.9}Ni_{0.1}O$. At a more positive side (0 to +0.8 V), bubbling can be seen in both electrodes due to the oxygen evolution reaction (OER). In the negative direction from 0 to −0.8 V, a featureless CV response with considerable reduction current at −0.8 V is seen. Once the range is extended to −0.9 and −1 V, a bubbling can be observed due to the hydrogen evolution reaction (HER) in both the electrodes. Similar explanation holds true for CuO also; however, the current densities are significantly lower than those in the Ni-doped systems (Figure S4c). Following from the results, the potential range is fixed from −0.8 to +0.4 V vs Ag/AgCl, to avoid OER/HER electrochemical reactions.

Electrocatalytic CO_2 Reduction. To examine the catalytic activity of all of the prepared electrodes for CO_2 electroreduction, CV experiments were carried out in the N_2- (blank) and CO_2-saturated (purging for 30 min) 0.5 M $NaHCO_3$ electrolyte at 20 mV s^{-1}. All of the CV experiments are carried out in the potential range of 0.0 to −0.8 V vs Ag/AgCl. Comparative CV responses of CuO (Figure 4a), $Cu_{0.95}Ni_{0.05}O$ (Figure 4b), and $Cu_{0.9}Ni_{0.1}O$ (Figure 4c) are shown in CO_2- and N_2-saturated solutions. The blank GCE response is also given with all of the catalysts for comparison. In the presence of CO_2, a broad cathodic response due to the electroreduction of CO_2 starts at an onset potential of about −0.54 V on CuO (Figure 4a). In $Cu_{0.95}Ni_{0.05}O$, the cathodic current in CO_2-saturated electrolytes is 0.18 mA, which is about 9 times higher than that in the N_2-saturated electrolyte (Figure 4b). Similarly, in $Cu_{0.9}Ni_{0.1}O$, the cathodic response with an onset voltage of −0.35 V is attained (Figure 4c). The onset voltage is about 20 mV lower than that for undoped CuO, demonstrating the catalytic effect of Ni^{2+} in CuO. The cathodic current at −0.8 V is 2.9 mA in CO_2-saturated solution. This is about 14 times higher than that in N_2-saturated solution, confirming the high activity of $Cu_{0.9}Ni_{0.1}O$ for CO_2 electroreduction. Current density after normalizing the surface area gives about 20 times higher activity in the case of $Cu_{0.9}Ni_{0.1}O$ compared to CuO. Similar enhancement is about 15 times in the case of $Cu_{0.95}Ni_{0.05}O$ compared to CuO. Interestingly, pure NiO is noncatalytic toward CO_2 electroreduction and shows almost no change in current in the CO_2-saturated electrolyte compared to that in the N_2-saturated electrolyte (Figure S5a). To ascertain that the catalysis is truly due to the substituted Ni^{2+} and Cu^{2+} interaction, the CV experiments with NiO-supported CuO (NiO/CuO) and Ni-metal supported CuO (Ni/CuO) are also carried out (Figure S5b,c). The CO_2 electroreduction current with NiO/CuO is 0.125 mA at −0.8 V. It is 0.06 mA with the Ni/CuO catalyst. Current values over supported catalysts are much lower than those over the Ni-substituted catalysts ($Cu_{0.95}Ni_{0.05}O$ and $Cu_{0.9}Ni_{0.1}O$). These observations indicate that synergetic ionic interaction between Cu^{2+} and Ni^{2+} is indeed is the major contributor for the observed enhanced activity. NiO/CuO and Ni/CuO are, on the other hand, minor contributors. Further, the estimated BET surface areas of $Cu_{0.95}Ni_{0.05}O$ and $Cu_{0.9}Ni_{0.1}O$ are about 5 times lower than those of CuO; therefore, the high activity of the doped compounds is truly due to ionically substituted Ni in CuO. All of the current values as a result of CO_2 electroreduction are normalized and compared with respect to BET surface areas (Table S2). Clearly, doped compounds are remarkably more active than CuO, Ni/CuO, and NiO/CuO, further highlighting the importance of the ionic interaction for superior activity.

Steady-state current responses for all of the three catalysts in the CO_2-saturated electrolyte at −0.8 V vs Ag/AgCl (−0.2 V RHE) are shown in Figure 4d. Initially, the current decreased gradually up to 400 s and attained a steady state with current values of 5.6 mA and 4.8 mA for $Cu_{0.9}Ni_{0.1}O$ and $Cu_{0.95}Ni_{0.05}O$, respectively. This indicates that both the catalysts are stable and $Cu_{0.9}Ni_{0.1}O$ has higher electroreduction activity for CO_2. In contrast, CuO initially showed a characteristic decrease followed by an increase in current, depicting an oxidation behavior. The steady state is not attained even after 1000 s due to the instability of CuO. In addition, CV is carried out after this chronoamperometric experiment for $Cu_{0.9}Ni_{0.1}O$ and CuO (Figure S6). It is observed that the redox behavior of $Cu_{0.9}Ni_{0.1}O$ is preserved, whereas it is diminished in CuO. This highlights that the Ni^{2+} substitution in CuO on one hand increases the activity and on the other hand imparts stability.

To analyze the products formed after CO_2 reduction, the evolved gases were collected by an air-lock syringe and the products were subjected to gas chromatography. The major gaseous products on all three electrocatalysts are CO, CH_4, C_2H_4, and H_2. The liquid sample was also collected and subjected to GC equipped with a liquid detection system. Exclusively, ethanol was detected. Since most of the copper-based electrocatalysts have been known to result in the formation of CH_4 and C_2H_4 with H_2 as the side product, it is interesting to note that Ni substitution in CuO suppresses the hydrogen production significantly. This is also depicted in terms of percent Faradaic efficiencies (FE %) for majorly gaseous products as shown in Figure 4e,f. FE % of CO is same (1.0%) for all of the three catalysts as the copper-based catalysts do not favor CO formation.[32] Comparatively, the formation of CH_4 and C_2H_4 predominantly occurs with FE % up to 29.4 and 12.8%, respectively, on $Cu_{0.9}Ni_{0.1}O$ (Figure 4e) and 20.2 and 8.7% for $Cu_{0.95}Ni_{0.05}O$. On CuO, the FE% for CH_4 and C_2H_4 is 3 and 4 times lower than on $Cu_{0.9}Ni_{0.1}O$. Inferior hydrocarbon FE % with CuO is due to the undesired HER and possibly a different mechanism. The FE % for ethanol was 15.3% on $Cu_{0.9}Ni_{0.1}O$ giving the total faradaic efficiency of 83.7%. FE % for hydrogen on $Cu_{0.95}Ni_{0.05}O$ and $Cu_{0.9}Ni_{0.1}O$ is 25.4 and 28.7%, much lower than on CuO (35.9%) as in Figure 4f. Thus, the presence of Ni in the CuO host enhances the formation of hydrocarbons while suppressing the hydrogen production.

Comparative electrocatalytic performance of the $Cu_{0.9}Ni_{0.1}O$ catalyst with the literature is available in Table S3 (Supporting Information). From the table, it is also clear that the hydrocarbon efficiency of the doped catalyst is comparable or better at much lower applied potential. Total FE % is 58−68% for both the Ni-substituted catalysts when only the gaseous products are analyzed. Very importantly, both $Cu_{0.95}Ni_{0.05}O$ and $Cu_{0.9}Ni_{0.1}O$ are able to generate hydrocarbons at −0.2 V (RHE), which is so far the lowest. In terms of overpotential, this is about 370 mV for methane and 280 mV for ethylene. To the best of our knowledge, this is the lowest overpotential ever reported. From Table S3, the lowest

DOI: 10.1021/acssuschemeng.9b05087
ACS Sustainable Chem. Eng. 2020, 8, 179−189

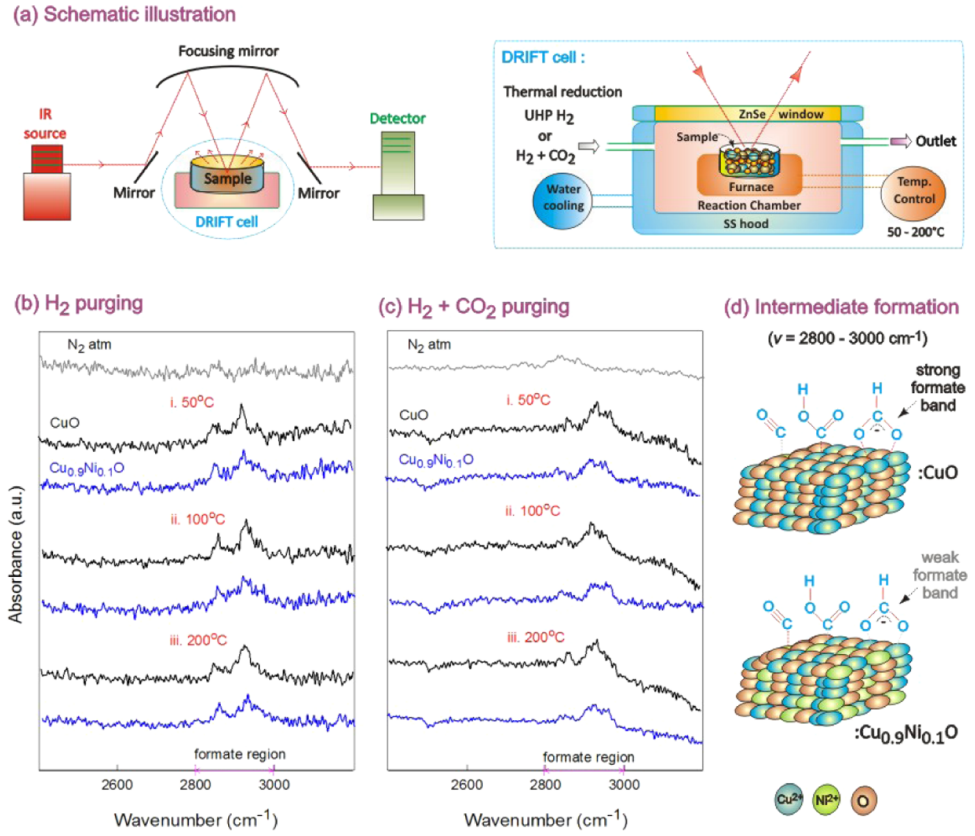

Figure 5. Schematic representation of DRIFT-FTIR spectroscopy (a), DRIFT spectra recorded in the IR range 2400−3200 cm^{-1} on passing H_2 (b) and CO_2 + H_2 UHP (c) gases over KBr-mixed $Cu_{0.9}Ni_{0.1}O$ and CuO catalysts at different temperatures from 50 to 200 °C. Possible intermediates formed on pure copper oxide (CuO) and nickel-doped copper oxide catalysts (d).

potential is −1.1 V (RHE) for methane and ethylene production. This is higher by 0.9 V than that for $Cu_{0.95}Ni_{0.05}O$ and $Cu_{0.9}Ni_{0.1}O$, a very significant gain in voltage. The materials used in this study are highly crystalline bulk materials. Clearly, apart from ionic interaction, crystallinity is possibly another important factor that reduces the overvoltage for this reaction.

The stability of $Cu_{0.9}Ni_{0.1}O$ catalyst is studied by depositing it onto a fluorine-doped tin oxide (FTO) electrode and subjecting to post-XRD and XPS after chronoamperometry in CO_2-saturated solution for 1000 s (Figures S7 and S8). It is observed that apart from FTO peaks, $Cu_{0.9}Ni_{0.1}O$ peaks are retained before and after CO_2 electrocatalysis, confirming the stability of the bulk structure of the $Cu_{0.9}Ni_{0.1}O$ catalyst (Figure S7). XPS also confirms the stability of the $Cu_{0.9}Ni_{0.1}O$ catalyst surface as shown in Figure S8. XPS data of as-prepared catalysts is also given for comparison. It is worth noticing that there is no change in the XPS spectra before and after chronoamperometry. Both copper and nickel show same oxidation states before and after the experiments, proving the stability of $Cu_{0.9}Ni_{0.1}O$ catalysts.

To access the stability under a more rigorous reductive treatment, CuO and $Cu_{0.9}Ni_{0.1}O$ were subjected to chronoamperometry at −0.8 V for 2 h. The CV after this treatment is shown in Figure S9. The behavior in both the materials confirms the formation of metallic copper.[44] This behavior confirms that the catalysts are unstable under long reductive treatment.

It is speculated that improvement in hydrocarbon selectivity along with the HER suppression is due to modification in the mechanism, which is investigated by in situ FTIR and DFT studies. Mechanistic investigation for the CO_2 electroreduction pathways over CuO and $Cu_{0.9}Ni_{0.1}O$ is executed using DRIFT in situ FTIR experiments (Figure 5). The schematic representation of the DRIFT cell is displayed in Figure 5a. As the copper-based materials are known for converting CO_2 to hydrocarbons both thermally and electrochemically, it is assumed that thermal reduction of CO_2 with gaseous hydrogen is similar to electrochemical reduction of CO_2. First, the interaction of H_2 over CuO and $Cu_{0.9}Ni_{0.1}O$ is investigated in the range of 2400−3200 cm^{-1} (Figure 5b). IR spectra of both as-prepared samples show no indication of any band in the flow of nitrogen at room temperature. On passing H_2, the DRIFT spectra of $Cu_{0.9}Ni_{0.1}O$ show weak bands in the range of 2800−3000 cm^{-1} at 50 °C. This band is due to the formation of formate on the surface by utilizing the atmospheric CO_2.[45] The similar band on CuO is considerably higher than that on $Cu_{0.9}Ni_{0.1}O$ under the same conditions. The same band at 100 °C shows an increase in the intensity on both the catalysts, but intensity is still higher on CuO. At 200 °C, the intensity of formate diminishes significantly over $Cu_{0.9}Ni_{0.1}O$ but not much change is observed in the case of CuO. Temperature higher than 300 °C causes complete disappearance of the formate band on both the catalysts (Figure S10). To be precise, the formate band disappears at 400 °C on $Cu_{0.9}Ni_{0.1}O$ and at 500 °C on CuO.

These experimental observations suggest that formate bands are more stable and prominent on the CuO surface than on $Cu_{0.9}Ni_{0.1}O$. Once Ni is substituted in the CuO matrix, the formate band is less stable and less prominent. Similar

DOI: 10.1021/acssuschemeng.9b05087
ACS Sustainable Chem. Eng. 2020, 8, 179−189

observation can also be drawn when the mixture of H_2 and CO_2 (1:1) is reacted on the catalyst's surface (Figure 5c). In this case also, the overall intensity of the formate band is less prominent on $Cu_{0.9}Ni_{0.1}O$ compared to CuO. Intensity differences in the formate can be prominently observed at 100, 200, and 300 °C.

In light of above observations, one can confirm that Ni substitution in CuO affects the catalyst's ability to stabilize formate (Figure 5d). This demonstrates the mechanistic differences between the two catalysts in which CuO shows the dominant formate pathway compared to $Cu_{0.9}Ni_{0.1}O$. Dominance of formate pathway with the generation of H_2 can be correlated well in light of quantum mechanical calculations carried out by Cheng et al.[46] This study reveals two pathways in copper-based materials, one is dominatingly forming formate and other forming CO. The pathway leading to CO eventually leads to hydrocarbon formation, while more formate leads to more hydrogen. This correlates well with the FTIR studies establishing that Ni substitution in CuO shows less contribution from the formate pathway, resulting in less hydrogen formation and due to this more hydrocarbons. CuO on the other hand shows more contribution from the formate pathway, resulting into fewer hydrocarbons and more hydrogen generation.

Further, density functional theory (DFT) was used for theoretical calculations (Figure 6), implemented in the CO_2 electroreduction pathways on CuO and $Cu_{0.9}Ni_{0.1}O$ model catalysts (Figures S11–S13). The optimized lattice parameters of bulk monoclinic CuO (space group—$C2/c$) were found to be a = 4.37, b = 3.86, and c = 3.92 Å (Figures S11 and S12), in excellent agreement with previous reports.[47,48] The (111) facet of CuO was chosen for calculations, as it has been found to be the most stable facet of CuO with lowest surface energy.[47] It contained 128 (64 Cu and 64 O) atoms. The Ni-doped structure contained 60 Cu and 4 Ni atoms, so the stoichiometry of alloy turned out to be $Cu_{0.9375}Ni_{0.0625}O$ (Figure S13). Only one composition of Ni doping was taken, as it is enough to observe the qualitative effect of change in the catalytic activity upon alloying.

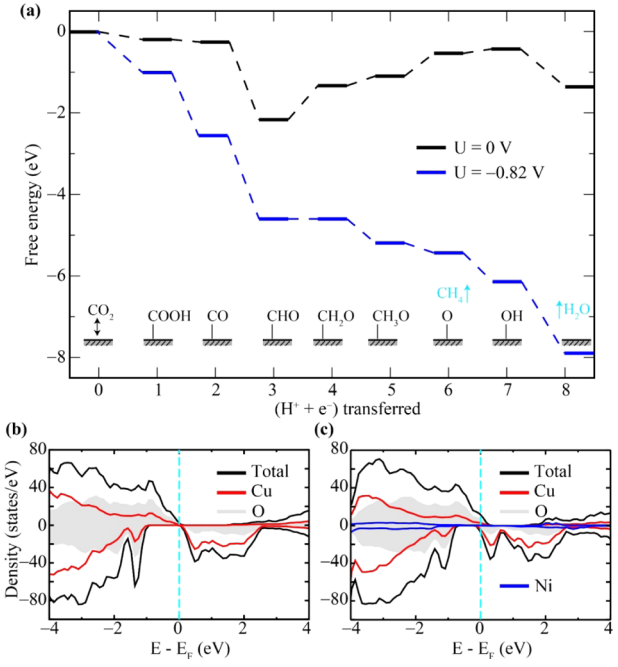

Figure 6. Free energy diagram for CO_2 electroreduction to CH_4 on the (111) surface of $Cu_{0.9375}Ni_{0.0625}O$ (a). Partial density of states (PDOS) of (111) surfaces of CuO (b) and $Cu_{0.9375}Ni_{0.0625}O$ (c).

The carbon dioxide electroreduction to methane formation involves seven intermediates (8-electron transfer process).[49] The (111) surface of CuO contains four types of active sites—coordinatively saturated Cu (Cu_{CSA}), coordinatively unsaturated Cu (Cu_{CUS}), surface O (O_{SUB}), and subsurface O (O_{SUF})[47] (Figure S11a). The *COOH, *CO, and *CHO intermediates that adsorb through C were relaxed on O_{SUF} sites, while those that bind through O (i.e., *CH_2O, *CH_3O, *O, and *OH) were relaxed on Cu_{CUS} sites (Figure S14), since Cu_{CUS} and O_{SUF} are more active than their corresponding saturated sites.[47] For the case of the (111) surface of $Cu_{0.9375}Ni_{0.0625}O$, we only relaxed these intermediates in the vicinity of the Ni atom as shown in Figure S15 to determine the effect of Ni doping. The intermediate adsorption energies (E_{ads}^{DFT}) were calculated for these completely relaxed structures using equations S1–S7. From these intermediate adsorption energies, Gibb's free energies of adsorption (G^*) were calculated according to the expression[50−52]

$$G^* = E_{ads}^{DFT} + \Delta ZPE - T\Delta S - eU \quad (2)$$

where ΔZPE, ΔS, e, and U are the difference in zero-point energies and vibrational entropies between reactants and products, number of electrons transferred, and applied potential, respectively. The value of temperature (T) has been taken to be 300 K. The values of E_{ads}^{DFT}, ZPE, and TS for reference molecules and intermediates are tabulated in Tables S4–S6.

The free energy diagrams for electroreduction of CO_2 to CH_4 on CuO and $Cu_{0.9375}Ni_{0.0625}O$ catalyst surfaces are shown in Figures 6a and S16, respectively, following the approach taken in previous reports.[50,52] The potential determining step (PDS) for this reaction is conversion of *CHO to *CH_2O on both pristine and doped catalyst surfaces, with $Cu_{0.9375}Ni_{0.0625}O$ exhibiting lower barrier for this step (0.82 eV) than the CuO catalyst (1.15 eV). Therefore, limiting potential (U_L), which is numerically equal to negative of the barrier of PDS,[50] values for CuO and $Cu_{0.9375}Ni_{0.0625}O$ catalysts come out to be −1.15 and −0.82 V, respectively. If the value of U_L is higher, the overall reaction becomes exergonic (i.e., downhill in free energy) at a lower external potential. Hence, the efficiency of CO_2 electroreduction to methane will be higher for $Cu_{0.9375}Ni_{0.0625}O$ as compared to the pristine CuO catalyst, in agreement with the experiments. The lower barrier for PDS observed in the case of $Cu_{0.9375}Ni_{0.0625}O$ can be explained from adsorption energies of *CHO and *CH_2O intermediates on the two catalysts as shown in Tables S5 and S6. The *CHO intermediate is more destabilized on the surface of $Cu_{0.9375}Ni_{0.0625}O$, while there is stabilization for the case of *CH_2O intermediate on its surface. The increased catalytic activity on the Ni-doped CuO can also be rationalized on the basis of change in electronic properties of CuO upon alloying. For this purpose, the partial density of states (PDOS) has been plotted for both surfaces in Figure 6b,c. The pristine CuO surface is a small-band-gap semiconductor with the valence band states mostly contributed by O and the conduction band states mostly contributed by Cu. The system becomes conducting upon doping with Ni; therefore, finite states present at the Fermi level are responsible for the

DOI: 10.1021/acssuschemeng.9b05087
ACS Sustainable Chem. Eng. 2020, 8, 179−189

increased activity of the Ni-doped CuO system, due to better interaction with the adsorbates.[53]

CONCLUSIONS

In summary, we have synthesized Ni-substituted CuO ($Cu_{1-x}Ni_xO$; x = 0.05 and 0.1) and CuO catalysts by the solution combustion method. Collective characterizations such as XRD, FESEM-EDS, HRTEM-STEM, EELS, EDS, and XPS conclude the bulk substitution of Ni^{2+} in the CuO host. Electrochemical studies of $Cu_{0.9}Ni_{0.1}O$ and $Cu_{0.95}Ni_{0.05}O$ show remarkable redox-active behavior and superior electrocatalytic activity compared to CuO, signifying the importance of substitution of ionic nickel. It is worth noticing that the electrocatalytic activities of $Cu_{0.9}Ni_{0.1}O$ and $Cu_{0.95}Ni_{0.05}O$ catalysts are superior to those of Ni metal and NiO-supported CuO. This proves that ionic interaction between Ni^{2+} and Cu^{2+} is vital for the high activity. Ni or NiO-supported CuO lacks this interaction and therefore it does not display high activity. Steady-state chronoamperometry at a fixed potential of −0.8 $V_{Ag/AgCl}$ (i.e., −0.2 V_{RHE}) in the CO_2-saturated electrolyte also revels high activity and stability of nickel-doped catalysts ($Cu_{0.9}Ni_{0.1}O$ and $Cu_{0.95}Ni_{0.05}O$). Remarkable improvement is noticed in the selectivity or faradaic efficiency of hydrocarbons. The FE % of H_2 on $Cu_{0.9}Ni_{0.1}O$ and $Cu_{0.95}Ni_{0.05}O$ was suppressed effectively compared to that on CuO. The observed hydrocarbon efficiency is achieved at the lowest possible overvoltage. A voltage gain of about 0.9 V is achieved compared to the reported catalysts. Simultaneously, the hydrocarbon selectivity is markedly improved. The FE % values of CH_4 and C_2H_4 are 29.4 and 12.8%, respectively, on $Cu_{0.9}Ni_{0.1}O$, which are about 3 and 4 times higher than those on CuO. These improvements are attributed to the mechanistic difference between substituted and unsubstituted catalysts. Mechanistic studies by the in situ DRIFT-FTIR infer that $Cu_{0.9}Ni_{0.1}O$ has fewer propensities toward formate intermediate compared to CuO. This leads to high hydrocarbon selectivity and lesser hydrogen formation. The free energy diagrams computed using DFT confirm that the Ni-doped CuO electrocatalyst is thermodynamically more active than pristine CuO, owing to its lower theoretical overpotential.

ASSOCIATED CONTENT

Supporting Information

The Supporting Information is available free of charge at https://pubs.acs.org/doi/10.1021/acssuschemeng.9b05087.

Experimental characterization like Reitveld refinements; CV responses of $Cu_{0.90}Ni_{0.10}O$, $Cu_{0.95}Ni_{0.05}O$, CuO (surface excess values), and Ni/NiO-deposited CuO; effect of scan rate and potential window; electrocatalytic reduction of CO_2 responses on NiO; Ni/NiO-deposited CuO catalysts; post-XRD, XPS, and CV data; DRIFT-FTIR spectra; normalized current density; and DFT calculation details with tabulations and comparative table for the electrocatalytic performance of the $Cu_{0.90}Ni_{0.10}O$ catalyst (PDF)

AUTHOR INFORMATION

Corresponding Author

*E-mail: ssharma@iitgn.ac.in.

ORCID

Subramanian Nellaiappan: 0000-0002-9318-2477
Silvia Irusta: 0000-0002-2966-9088
Jordan A. Hachtel: 0000-0002-9728-0920
Abhishek K. Singh: 0000-0002-7631-6744
Chandra Sekhar Tiwary: 0000-0001-9760-9768
Sudhanshu Sharma: 0000-0002-5217-9941

Author Contributions

S.S. and S.N. envisaged the idea and executed the experiments. R.K., A.K.S., and C.S.T. carried out DFT calculations. C.S. performed Reitveld refinement studies. S.I. performed XPS analysis. J.A.H. and J.C.I. performed the transmission microscopy experiments. All of the authors contributed to the data analysis and writing and gave approval for the final submission.

Notes

The authors declare no competing financial interest.

ACKNOWLEDGMENTS

S.S. and S.N. gratefully acknowledge IIT Gandhinagar and DST-SERB-sponsored research project (EMR/2016/000806) for funding and fellowship. A portion of the microscopy was performed as part of a user proposal at Oak Ridge National Laboratory's Center for Nanophase Materials Sciences (CNMS), which is a U.S. Department of Energy, Office of Science User Facility. R.K. and A.K.S. acknowledge computational facilities provided by Materials Research Centre, Solid State and Structural Chemistry Unit, and Supercomputer Education and Research Centre at Indian Institute of Science.

REFERENCES

(1) Kumar, B.; Brian, J. P.; Atla, V.; Kumari, S.; Bertram, K. A.; White, R. T.; Spurgeon, J. M. New Trends in the Development of Heterogeneous Catalysts for Electrochemical CO_2 Reduction. *Catal. Today* **2016**, *270*, 19−30.

(2) Zhu, D. D.; Liu, J. L.; Qiao, S. Z. Recent Advances in Inorganic Heterogeneous Electrocatalysts for Reduction of Carbon Dioxide. *Adv. Mater.* **2016**, *28*, 3423−3452.

(3) Porosoff, M. D.; Yan, B.; Chen, J. G. Catalytic Reduction of CO_2 by H_2 for Synthesis of CO, Methanol and Hydrocarbons: Challenges and Opportunities. *Energy Environ. Sci.* **2016**, *9*, 62−73.

(4) Boston, D. J.; Xu, C.; Armstrong, D. W.; MacDonnell, F. M. Photochemical Reduction of Carbon Dioxide to Methanol and Formate in a Homogeneous System with Pyridinium Catalysts. *J. Am. Chem. Soc.* **2013**, *135*, 16252−16255.

(5) Richardson, R. D.; Holland, E. J.; Carpenter, B. K. A Renewable Amine for Photochemical Reduction of CO_2. *Nat. Chem.* **2011**, *3*, 301−303.

(6) Yang, N.; Waldvogel, S. R.; Jiang, X. Electrochemistry of Carbon Dioxide on Carbon Electrodes. *ACS Appl. Mater. Interfaces* **2016**, *8*, 28357−28371.

(7) Qiao, J.; Liu, Y.; Hong, F.; Zhang, J. A Review of Catalysts for the Electroreduction of Carbon Dioxide to Produce Low-carbon Fuels. *Chem. Soc. Rev.* **2014**, *43*, 631−675.

(8) Britovsek, G. J. P.; Bruce, M.; Gibson, V. C.; Kimberley, B. S.; Maddox, P. J.; Mastroianni, S.; McTavish, S. J.; Redshaw, C.; Solan, G. A.; Strömberg, S.; White, A. J. P.; Williams, D. J. Iron and Cobalt Ethylene Polymerization Catalysts Bearing 2,6-Bis(Imino)Pyridyl Ligands: Synthesis, Structures, and Polymerization Studies. *J. Am. Chem. Soc.* **1999**, *121*, 8728−8740.

(9) Wang, Z.-L.; Li, C.; Yamauchi, Y. Nanostructured Nonprecious Metal Catalysts for Electrochemical Reduction of Carbon Ddioxide. *Nano Today* **2016**, *11*, 373−391.

(10) Hossain, M. N.; Wen, J.; Konda, S. K.; Govindhan, M.; Chen, A. Electrochemical and FTIR Spectroscopic Study of CO_2Reduction at a Nanostructured Cu/Reduced Graphene Oxide Thin Film. *Electrochem. Commun.* **2017**, *82*, 16−20.

DOI: 10.1021/acssuschemeng.9b05087
ACS Sustainable Chem. Eng. 2020, 8, 179−189

(11) Chen, C. S.; Handoko, A. D.; Wan, J. H.; Ma, L.; Ren, D.; Yeo, B. S. Stable and Selective Electrochemical Reduction of Carbon Dioxide to Ethylene on Copper Mesocrystals. *Catal. Sci. Techno.* **2015**, *5*, 161−168.
(12) Kuhl, K. P.; Cave, E. R.; Abram, D. N.; Jaramillo, T. F. New Insights into the Electrochemical Reduction of Carbon Dioxide on Metallic Copper Surfaces. *Energy Environ. Sci.* **2012**, *5*, 7050−7059.
(13) Hori, Y.; Takahashi, R.; Yoshinami, Y.; Murata, A. Electrochemical Reduction of CO_2 at a Copper Electrode. *J. Phys. Chem. B* **1997**, *101*, 7075−7081.
(14) Kudo, A.; Nakagawa, S.; Tsuneta, A.; Sakata, T. Electrochemical Reduction of High Pressure CO_2on Ni Electrodes. *J. Electrochem. Soc.* **1993**, *140*, 1541−1545.
(15) Zhu, W.; Zhang, Y. J.; Zhang, H.; Lv, H.; Li, Q.; Michalsky, R.; Peterson, A. A.; Sun, S. Active and Selective Conversion of CO_2 to CO on Ultrathin Au Nanowires. *J. Am. Chem. Soc.* **2014**, *136*, 16132−16135.
(16) Kim, C.; Eom, T.; Jee, M. S.; Jung, H.; Kim, H.; Min, B. K.; Hwang, Y. J. Insight into Electrochemical CO_2 Reduction on Surface-Molecule-Mediated Ag Nanoparticles. *ACS Catal.* **2017**, *7*, 779−785.
(17) Zhang, S.; Kang, P.; Meyer, T. J. Nanostructured Tin Catalysts For Selective Electrochemical Reduction of Carbon Dioxide To Formate. *J. Am. Chem. Soc.* **2014**, *136*, 1734−1737.
(18) Detweiler, Z. M.; White, J. L.; Bernasek, S. L.; Bocarsly, A. B. Anodized Indium Metal Electrodes For Enhanced Carbon Dioxide Reduction In Aqueous Electrolyte. *Langmuir* **2014**, *30*, 7593−7600.
(19) Gao, D.; Zhou, H.; Wang, J.; Miao, S.; Yang, F.; Wang, G.; Bao, X. Size-dependent Electrocatalytic Reduction of CO_2 Over Pd Nanoparticles. *J. Am. Chem. Soc.* **2015**, *137*, 4288−4291.
(20) Kim, D.; Resasco, J.; Yu, Y.; Asiri, A. M.; Yang, P. Synergistic Geometric And Electronic Effects For Electrochemical Reduction Of Carbon Dioxide Using Gold-Copper Bimetallic Nanoparticles. *Nat. Commun.* **2014**, *5*, No. 4948.
(21) Rasul, S.; Anjum, D. H.; Jedidi, A.; Minenkov, Y.; Cavallo, L.; Takanabe, K. A Highly Selective Copper-Indium Bimetallic Electrocatalyst For The Electrochemical Reduction Of Aqueous CO_2 to CO. *Angew. Chem., Int. Ed. Engl.* **2015**, *54*, 2146−2150.
(22) Ren, D.; Ang, B. S.-H.; Yeo, B. S. Tuning the Selectivity of Carbon Dioxide Electroreduction toward Ethanol on Oxide-Derived Cu_xZn Catalysts. *ACS Catal.* **2016**, *6*, 8239−8247.
(23) Clark, E. L.; Hahn, C.; Jaramillo, T. F.; Bell, A. T. Electrochemical CO_2 Reduction over Compressively Strained CuAg Surface Alloys with Enhanced Multi-Carbon Oxygenate Selectivity. *J. Am. Chem. Soc.* **2017**, *139*, 15848−15857.
(24) Chen, D.; Yao, Q.; Cui, P.; Liu, H.; Xie, J.; Yang, J. Tailoring the Selectivity of Bimetallic Copper−Palladium Nanoalloys for Electrocatalytic Reduction of CO_2 to CO. *ACS Appl. Energy Mater.* **2018**, *1*, 883−890.
(25) Mandal, L.; Yang, K. R.; Motapothula, M. R.; Ren, D.; Lobaccaro, P.; Patra, A.; Sherburne, M.; Batista, V. S.; Yeo, B. S.; Ager, J. W.; Martin, J.; Venkatesan, T. Investigating the Role of Copper Oxide in Electrochemical CO_2 Reduction in Real Time. *ACS Appl. Mater. Interfaces* **2018**, *10*, 8574−8584.
(26) Ren, D.; Deng, Y.; Handoko, A. D.; Chen, C. S.; Malkhandi, S.; Yeo, B. S. Selective Electrochemical Reduction of Carbon Dioxide to Ethylene and Ethanol on Copper(I) Oxide Catalysts. *ACS Catal.* **2015**, *5*, 2814−2821.
(27) Chi, D.; Yang, H.; Du, Y.; Lv, T.; Sui, G.; Wang, H.; Lu, J. Morphology-controlled CuO Nanoparticles for Electroreduction of CO_2 to Ethanol. *RSC Adv.* **2014**, *4*, 37329−37332.
(28) Yano, J.; Morita, T.; Shimano, K.; Nagami, Y.; Yamasaki, S. Selective Ethylene Formation By Pulse-Mode Electrochemical Reduction Of Carbon Dioxide Using Copper And Copper-Oxide Electrodes. *J. Solid State Electrochem.* **2006**, *11*, 554−557.
(29) Eilert, A.; Cavalca, F.; Roberts, F. S.; Osterwalder, J.; Liu, C.; Favaro, M.; Crumlin, E. J.; Ogasawara, H.; Friebel, D.; Pettersson, L. G.; Nilsson, A. Subsurface Oxygen in Oxide-Derived Copper Electrocatalysts for Carbon Dioxide Reduction. *J. Phys. Chem. Lett.* **2017**, *8*, 285−290.
(30) Handoko, A. D.; Chan, K. W.; Yeo, B. S. −CH3 Mediated Pathway for the Electroreduction of CO_2 to Ethane and Ethanol on Thick Oxide-Derived Copper Catalysts at Low Overpotentials. *ACS Energy Lett.* **2017**, *2*, 2103−2109.
(31) Li, C. W.; Kanan, M. W. CO_2Reduction At Low Overpotential on Cu Electrodes Resulting from the Reduction of Thick Cu_2O Films. *J. Am. Chem. Soc.* **2012**, *134*, 7231−7234.
(32) Li, Q.; Fu, J.; Zhu, W.; Chen, Z.; Shen, B.; Wu, L.; Xi, Z.; Wang, T.; Lu, G.; Zhu, J. J.; Sun, S. Tuning Sn-Catalysis for Electrochemical Reduction of CO_2 to CO via the Core/Shell Cu/SnO_2 Structure. *J. Am. Chem. Soc.* **2017**, *139*, 4290−4293.
(33) Huo, S.; Weng, Z.; Wu, Z.; Zhong, Y.; Wu, Y.; Fang, J.; Wang, H. Coupled Metal/Oxide Catalysts with Tunable Product Selectivity for Electrocatalytic CO_2 Reduction. *ACS Appl. Mater. Interfaces* **2017**, *9*, 28519−28526.
(34) Zhao, Y.; Wang, C.; Wallace, G. G. Tin Nanoparticles Decorated Copper Oxide Nanowires for Selective Electrochemical Reductionof Aqueous CO_2 to CO. *J. Mater. Chem. A* **2016**, *4*, 10710−10718.
(35) Upham, D. C.; Derk, A. R.; Sharma, S.; Metiu, H.; McFarland, E. W. CO_2Methanation by Ru-doped Ceria: The Role of the Oxidation State of the Surface. *Catal. Sci. Technol.* **2015**, *5*, 1783−1791.
(36) Hegde, M. S.; Madras, G.; Patil, K. C. Noble Metal Ionic Catalysts. *Acc. Chem. Res.* **2009**, *42*, 704−712.
(37) Kresse, G.; Hafner, J. Ab initio Molecular Dynamics for Liquid Metals. *Phys. Rev. B* **1993**, *47*, 558−561.
(38) Dudarev, S. L.; Botton, G. A.; Savrasov, S. Y.; Humphreys, C. J.; Sutton, A. P. Electron-Energy-Loss Spectra and the Structural Stability of Nickel Oxide: An LSDA1+U Study. *Phys. Rev. B* **1998**, *57*, 1501−1509.
(39) Perdew, J. P.; Burke, K.; Ernzerho, M. Generalized Gradient Approximation Made Simple. *Phys. Rev. Lett.* **1996**, *77*, 3865−3868.
(40) Van De Walle, A. A.; Astaa, M.; Cederb, G. The Alloy Theoretic Automated Toolkit: A User Guide. *Calphad* **2002**, *26*, 539−553.
(41) Dubale, A. A.; Pan, C.-J.; Tamirat, A. G.; Chen, H.-M.; Su, W.-N.; Chen, C.-H.; Rick, J.; Ayele, D. W.; Aragaw, B. A.; Lee, J.-F.; Yang, Y.-W.; Hwang, B.-J. Heterostructured Cu_2O/CuO Decorated with Nickel as a Highly Efficient Photocathode for Photoelectrochemical Water Reduction. *J. Mater. Chem. A* **2015**, *3*, 12482−12499.
(42) Naghash, A. R.; Etsell, T. H.; Xu, S. XRD and XPS Study of Cu-Ni Interactions on Reduced Copper-Nickel-Aluminum Oxide Solid Solution Catalysts. *Chem. Mater.* **2006**, *18*, 2480−2488.
(43) Bard, A. J.; Faulkner, L. R. *Electrochemical Methods: Fundamentals and Applications*, 2nd ed.; Wiley: NY: 2009.
(44) Singh, R. P.; Arora, P.; Nellaiappan, S.; Shivakumara, C.; Paliwal, M.; Sharma, S. Electrochemical Insights into Layered La_2CuO_4 Perovskite: Redox Active Ionic Copper for Selective CO_2 Electroreduction. *Electrochim. Acta* **2019**, *326*, 134952−134963.
(45) Sharma, S.; Sravan Kumar, K. B.; Chandnani, Y. M.; Phani Kumar, V. S.; Gangwar, B. P.; Singhal, A.; Deshpande, P. A. Mechanistic Insights into CO2 Methanation over Ru-Substituted CeO_2. *J. Phys. Chem. C* **2016**, *120*, 14101−14112.
(46) Cheng, T.; Xiao, H.; Goddard, W. A. Reaction Mechanisms for the Electrochemical Reduction of CO_2 to CO and Formate on the Cu(100) Surface at 298K from Quantum Mechanics Free Energy Calculations with Explicit Water. *J. Am. Chem. Soc.* **2016**, *138*, 13802−13805.
(47) Mishra, A. K.; Roldan, A.; Leeuw, N. H. D. CuO Surfaces and CO_2 Activation: A Dispersion-Corrected DFT+ U Study. *J. Phys. Chem. C* **2016**, *120*, 2198−2214.
(48) Heinemann, M.; Eifert, B.; Heiliger, C. Band Structure and Phase Stability of the Copper Oxides Cu_2O, CuO, and Cu_4O_3. *Phys. Rev. B* **2013**, *87*, 115111−115115.
(49) Ahmad, R.; Singh, A. K. Synergistic Core−shell Interactions Enable Ultra-low Overpotentials for Enhanced CO_2 Electro-reduction Activity. *J. Mater. Chem. A* **2018**, *6*, 21120−21130.

DOI: 10.1021/acssuschemeng.9b05087
ACS Sustainable Chem. Eng. 2020, 8, 179−189

(50) Peterson, A. A.; Abild-Pedersen, F.; Studt, F.; Rossmeisl, J.; Norskov, J. K. How Copper Catalyzes the Electroreduction of Carbon Dioxide into Hydrocarbon Fuels. *Energy Environ. Sci.* **2010**, *3*, 1311−1315.
(51) Kumar, R.; Das, D.; Singh, A. K. C2N/WS2 van der Waals Type-II Heterostructure as a Promising Water Splitting Photocatalyst. *J. Catal.* **2018**, *359*, 143−150.
(52) Gao, D.; Zhou, H.; Wang, J.; Miao, S.; Yang, F.; Wang, G.; Wang, J.; Bao, X. Size-Dependent Electrocatalytic Reduction of CO_2 over Pd Nanoparticles. *J. Am. Chem. Soc.* **2015**, *137*, 4288−4291.
(53) Ruban, A.; Hammer, B.; Stoltze, P.; Skriver, H. L.; Norskov, J. K. Surface Electronic Structure and Reactivity of Transition and Noble Metals. *J. Mol. Catal. A: Chem.* **1997**, *115*, 421−429.

DOI: 10.1021/acssuschemeng.9b05087
ACS Sustainable Chem. Eng. 2020, 8, 179−189